Research Square

Preprints are preliminary reports that have not undergone peer review.
They should not be considered conclusive, used to inform clinical practice,
or referenced by the media as validated information.

Enhanced Electrocatalytic Oxygen Reduction to H_2O with High Selectivity via 2D 1T-MoS_2 Integrated with Functionalized Carbon Nanohorns

mengjiao wang

mengjiao.wang@polito.it

Politecnico di Torino

Stefania Benazzato

University of Padua

Łukasz Cieszyński

University of Warsaw

Matteo Crisci

Justus-Liebig-Universität Gießen

Micaela Pozzati

Politecnico di Torino

Laura Calvillo

University of Padua

Yongying Wang

Politecnico di Torino

Yazhou Zhou

VSB - Technical University of Ostrava

Enzo Menna

University of Padua

Silvio Osella

University of Warsaw

Juqin Zeng

Politecnico di Torino

Teresa Gatti

Politecnico di Torino

Article

Keywords:

Posted Date: July 13th, 2026

DOI: https://doi.org/10.21203/rs.3.rs-10153401/v1

License: This work is licensed under a Creative Commons Attribution 4.0 International License.
Read Full License

Additional Declarations: No competing interests reported.

Abstract

Developing cost-effective and high-performance electrocatalysts for the oxygen reduction reaction (ORR) is essential for advancing anion-exchange membrane fuel cell technologies. In this study, we report a robust heterostructure formed by covalently functionalized carbon nanohorns (CNH-N) integrated with metallic 1T-MoS_2 2D nanosheets. Through tailored diazonium chemistry, positively charged ammonium groups were introduced onto CNHs, enabling strong electrostatic and van der Waals interactions with negatively charged exfoliated MoS_2. Structural and spectroscopic analyses confirm successful functionalization, enhanced defect modulation, and intimate CNH–MoS_2 coupling. The resulting CNH-N-MoS_2 catalyst exhibits remarkable ORR performance, including an optimized onset potential of 0.80 V, reduced charge-transfer resistance, and a dominant four-electron reduction pathway with ~ 94% selectivity toward H_2O, which is comparable to commercial Pt/C. These results highlight how controlled chemical functionalization and heterointerface engineering can synergistically enhance catalytic activity and stabilize the 1T-MoS_2 phase. The CNH-N-MoS_2 heterostructures thus represent a promising class of metal-free/low-metal-content electrocatalysts for efficient fuel cell applications.

Introduction

The development of anion-exchange membrane fuel cells (AEMFCs) is considered an important step toward a sustainable energy future owing to their safe operation, low environmental impact, and potential for energy-efficient electricity generation. However, the sluggish kinetics of the oxygen reduction reaction (ORR) at the cathode, together with the possibility of incomplete oxygen reduction, significantly limits the efficiency and performance of AEMFCs. [1] Consequently, the development of highly active and selective ORR electrocatalysts capable of promoting the complete four-electron reduction of O_2 to H_2O at low overpotentials has become a major research focus. Platinum-based catalysts remain the benchmark ORR catalysts because of their exceptional activity and stability, yet their high cost severely restricts the large-scale commercialization of fuel-cell technologies.[2] As a result, considerable efforts have been devoted to developing low-cost platinum-group-metal-free electrocatalysts.

Among the various candidates investigated, two-dimensional (2D) transition metal dichalcogenides (TMDCs) have emerged as promising ORR electrocatalysts owing to their layered structures, high surface area, tunable electronic properties, and abundance of catalytically active sites. [3,4] In particular, MoS_2 has attracted significant attention because of its low cost, scalability, and widespread availability.[5] Mass-produced MoS_2 nanosheets have already been employed as screen-printed ORR electrodes, highlighting their practical potential.[6] The catalytic performance of MoS_2 originates from its edge sites, basal-plane defects, and S vacancies, which facilitate oxygen adsorption and activation.[7–9] The high specific surface area of 2D MoS_2 also promotes mass transport and maximizes active-site exposure, while the metallic 1T phase exhibits enhanced electrical conductivity and accelerated charge-transfer kinetics compared with the semiconducting 2H phase.[10] Accordingly, the electrocatalytic properties can be tailored through doping, phase engineering, and heterostructure construction to optimize the

adsorption energies of ORR intermediates and increase the number of active sites.[11,12] For example, dopant engineering with Nb and Ta has been investigated, although these p-type dopants were found to negatively affect ORR activity.[13] In contrast, phase-engineered 1T/2H-MoS_2 exhibits superior performance owing to its improved conductivity and larger BET surface area, while hybrid systems combining MoS_2 with noble metals, Fe-based compounds, or Ni-based compounds have demonstrated enhanced activity and selectivity.[14–17] Despite these advances, the ORR performance of MoS_2 remains strongly dependent on catalyst design, and further improvements in activity, selectivity, and durability require a deeper understanding of the structure–property–activity relationships governing the reaction.

One particularly attractive strategy involves coupling MoS_2 with conductive carbon materials to exploit synergistic effects that improve electron transport, active-site utilization, and structural stability while avoiding the use of expensive or potentially hazardous components.[18,19] For example, abundant active sites of N-MoS_2/C derived from rich defects can enhance ORR activity, while the porous C is in charge of reducing the catalyst aggregation.[20] MoS_2/reduced graphene oxide (rGO) has been employed as catalyst or a platform for incorporating additional catalytic species such as Ni-based compounds.[21,22] The incorporation of electroactive N-doped graphene quantum dots into MoS_2/rGO nanohybrids further enhances ORR performance through favorable interfacial interactions and increased surface area and porosity.[23] Similarly, nitrogen-doped porous carbon sheets have been used to support MoS_2/SnS heterostructures, where the conductive carbon framework improves electron transfer and prevents catalyst agglomeration.[24] These studies clearly demonstrate the benefits of integrating MoS_2 with conductive carbon architectures.

Despite the above-mentioned carbon nanomaterials, carbon nanohorns (CNHs) have recently emerged as particularly promising building blocks for electrocatalytic applications. [25] CNHs are unique sp^2-hybridized carbon nanostructures composed of horn-shaped graphene tubules that self-assemble into spherical aggregates. In contrast to carbon nanotubes, whose functionalization often requires harsh chemical treatments, CNHs possess highly reactive five-membered-ring defects at their horn tips that facilitate efficient and homogeneous covalent modification. Moreover, their intrinsically porous three-dimensional architecture provides a large accessible surface area, efficient mass transport pathways, excellent electrical conductivity, and high chemical stability.[26] Recent advances in covalent chemistry have enabled the attachment of a variety of organic functionalities to CNHs, significantly improving their processability and expanding their application scope.[27] Nevertheless, examples of CNH-based hybrids with catalytically active nanostructures remain scarce. In particular, the integration of CNHs with TMDCs has received very limited attention, despite the complementary properties of these materials. While TMDCs offer abundant electrocatalytically active sites, they often suffer from limited conductivity, weak interfacial interactions, and structural restacking. The construction of CNH–TMDC heterostructures capable of efficiently catalyzing ORR therefore remains largely unexplored.

Motivated by these considerations, we envisioned that integrating metallic-phase 1T-MoS_2 nanosheets with the highly conductive and porous CNH framework could yield a robust 3D–2D heterostructure capable of efficiently catalyzing the four-electron ORR pathway toward H_2O. A critical aspect in the design of such CNH–MoS_2 electrocatalysts is the establishment of strong interfacial interactions between the two nanostructured components. Since neither pristine CNHs nor MoS_2 possess a sufficient density of dangling bonds for direct coupling, the introduction of suitable molecular linkers carrying complementary functionalities is required. In particular, the negatively charged exfoliated 1T-MoS_2 nanosheets necessitate a linker that can simultaneously interact with the π-conjugated surface of CNHs and provide positively charged functionalities capable of electrostatic association with MoS_2. Moreover, van der Waals and electrostatic interactions are expected to provide superior interfacial stability compared with weak van der Waals or supramolecular forces while simultaneously perturbing the electronic structure of the heterointerface, thereby influencing its electrocatalytic properties. Herein, we report the fabrication of a CNH–N–MoS_2 heterostructure through the functionalization of CNHs with 4-amino-N,N,N-trimethylbenzenaminium (TMA), which is covalently attached to the CNH surface and subsequently serves as an electrostatic anchor for negatively charged MoS_2 nanosheets (Fig. 1). The successive functionalization and assembly steps were systematically verified by thermogravimetric analysis (TGA), Raman spectroscopy, and transmission electron microscopy (TEM). The electrocatalytic activity of the resulting CNH–N–MoS_2 nanoconjugates toward ORR was then evaluated as a proof of concept. The results demonstrate that higher MoS_2 loadings lead to enhanced ORR performance, while the covalent attachment of TMA to CNHs and the electrostatic and van der Waals interaction with MoS_2 facilitate charge transfer across the heterointerface and increase the accessible catalytic surface area. As a result, the CNH–N–MoS_2 heterostructure exhibits excellent ORR selectivity, reaching 94%, highlighting the potential of engineered carbon–TMDC heterostructures for fuel-cell applications. Furthermore, density functional theory (DFT) calculations reveal that CNH functionalization induces electron-density redistribution within MoS_2 and that S sites located at the interface of metallic 1T-MoS_2 favor the four-electron ORR pathway, providing mechanistic insight into the origin of the enhanced catalytic activity.

Results and discussion

Structural characterization

Functionalized CNH-N were synthesized through a diazotization reaction (Fig. 1) based on an adapted Tour functionalization protocol, which has previously been employed to prepare soluble derivatives of various carbon nanostructures.[28–30] The aniline precursor, TMA iodide, was synthesized according to a reported literature procedure.[31] Due to the hydrophilicity of covalently bonded TMA, CNH-N exhibited excellent water dispersibility, reaching 1.431 mg mL^{-1}, whereas stable aqueous suspensions of pristine CNHs could not be obtained. The presence of charged ammonium groups is expected to enhance interactions with water while suppressing hydrophobic and π–π stacking interactions between

neighbouring CNHs, thereby increasing colloidal stability. The optical image in Fig. S1 shows the aqueous dispersion of CNH and CNH-N. CNH-N and exfoliated 1T-MoS_2 were subsequently mixed at a weight ratio of 10:1, resulting in the formation of the CNH-N–MoS_2 hybrid via electrostatic and van der Waals interactions.

To confirm the successful surface functionalization, thermogravimetric analysis (TGA) was performed on both pristine CNHs and functionalized CNH-N samples. The thermal stability of the materials was evaluated under a nitrogen atmosphere (Fig. 2a). Pristine CNHs exhibited excellent thermal stability, showing only 5.30% weight loss between 100 and 600°C, which could be attributed to the decomposition of oxygen containing groups derived from the manufacturing process or residual solvent molecules. In contrast, CNH-N displayed a significantly higher weight loss of 32.09% within the same temperature range, indicating the presence of additional thermally labile functionalities introduced during the functionalization process. Specifically, TGA/DTG profiles of CNH-N reveal a two-step degradation behavior. The first weight-loss stage, occurring below 200°C, is associated with the removal of physically adsorbed moisture and residual volatile species. The second degradation stage, centred at approximately 480°C, is attributed to the thermal decomposition of grafted organic moieties and surface functional groups.[31] Beyond 550°C, CNH-N exhibited remarkable thermal stability, retaining approximately 60% of its initial mass at 1000°C, which reflects the presence of a highly stable carbonaceous framework. The substantially greater mass loss observed for CNH-N compared with pristine CNHs is attributed to the decomposition of covalently attached organic functionalities. These results provide strong evidence for the successful functionalization of the CNH surface and confirm the incorporation of TMA onto the CNHs.

To gain further insight into the surface chemical composition and the nature of the introduced functional groups, X-ray photoelectron spectroscopy (XPS) analysis was performed on pristine CNHs and CNH-N samples (Fig. 2b and 2c). The analysis of the C 1s region of CNHs and CNH-N shows a main peak at 284.2 eV attributed to C sp^2 and a small component at 285.0 eV related to C sp^3 (Fig. 2b). In addition, weak peaks ascribed to oxygenated groups are detected, such as alcoholic (286.0 eV), carbonyl (287.9 eV) and carboxylic (288.9 eV) groups. Quantification of the C 1s peaks showed an increase in the sp^3 carbon contribution from 21.9% to 27.9% and a corresponding decrease in the sp^2 carbon contribution from 57.2% to 52.9%, indicating that functionalization increased the density of sp^3 defects while partially disrupting the sp^2 carbon framework. The analysis of the N 1s region confirms the CNH modification as CNH-N showing the expected $(CH_3)_3–N^+$ component at 402.4 eV (Fig. 2c). In addition, another component at 399.2 eV is observed, which could be attributed to –N = N– moieties. These azobenzene groups may be generated during the functionalization process either through diazo coupling between diazonium salts and surface-bound N,N,N-trimethylbenzylammonium groups, or via the radical decomposition of diazoanhydride intermediates formed during the Tour reaction mechanism.[29] It cannot be excluded a small presence of -NH_2 species from residual aniline overlapping with the –N = N– signal.

Dynamic light scattering (DLS) and ζ-potential measurements were performed to evaluate the colloidal properties of CNH-N and exfoliated 1T-MoS_2 and to assess the feasibility of electrostatic assembly between the two components. The aqueous dispersion of CNH-N exhibited a hydrodynamic diameter of 126.1 nm, indicating good dispersion of the functionalized carbon nanohorns and showing good agreement with previously reported values.[32–34] The corresponding polydispersity index (PdI) of 0.143 suggests a relatively narrow particle-size distribution. Further evidence for the successful functionalization of CNHs was provided by ζ-potential measurements, which revealed a value of + 36.9 mV. The positive value of ζ potential is associated to the presence of positively charged surface-bound quaternary ammonium groups, introduced during the functionalization process and indicates good colloidal stability of the dispersion.[29] To obtain a complementary negatively charged counterpart for electrostatic assembly, bulk MoS_2 was exfoliated via lithium intercalation using *n*-butyllithium, followed by hydration and ultrasonic dispersion in water, as previously reported by us.[35,36] This procedure yielded exfoliated 1T-MoS_2 nanosheets with a strongly negative surface charge, as confirmed by a ζ-potential value of approximately − 40 mV. The substantial difference in surface charge between CNH-N and 1T-MoS_2 promotes strong electrostatic attraction, facilitating the spontaneous assembly and stabilization of the CNH-N–MoS_2 hybrid material (Fig. 1). Therefore, the combination of covalent functionalization of CNHs and electrostatic self-assembly with negatively charged 1T-MoS_2 nanosheets represents an effective and versatile strategy for the fabrication of robust carbon–TMDC heterostructures.

Raman spectroscopy was employed to further verify the successful functionalization of CNHs and to investigate the van der Waals interaction between CNH-N and MoS_2. Measurements were performed using an excitation wavelength of 518 nm, which is resonant with the A-exciton transition of MoS_2. To minimize sample heating and avoid laser-induced damage, the laser power was limited to 0.3 mW cm^{-2} and the exposure time was set to 10 s. The Raman spectra of pristine CNHs and CNH-N exhibit three characteristic features: the D band at approximately 1319 cm^{-1}, arising from disorder-induced vibrations associated with sp^3 defects in the carbon framework; the G band at approximately 1590 cm^{-1}, corresponding to the in-plane vibrational mode of sp^2-hybridized carbon atoms; and the second-order 2D band located at around 2630 cm^{-1}. The intensity ratio between the D and G bands (I_D/I_G) is commonly used to evaluate the degree of structural disorder and the density of sp^3 defects in carbon nanomaterials.

For pristine CNHs, an I_D/I_G ratio of 1.22 ± 0.05 was obtained, whereas CNH-N exhibited an increased ratio of 1.60 ± 0.20. This increase indicates the introduction of additional sp^3 defects as a result of the covalent functionalization reaction with TMA groups. These findings are in good agreement with the XPS results. The relatively moderate increase in I_D/I_G suggests that, although covalent bonds are formed on the CNH surface, the overall graphitic framework remains largely preserved.[33,34] Upon assembly with MoS_2, the I_D/I_G ratio decreased to approximately 1.15. This behavior may be attributed to the passivation of pristine defect sites on the CNH surface by chemically introduced MoS_2. Exfoliated MoS_2 may preferentially interact with the defect sites on the CNH surface, effectively saturating these defects and

thereby reducing the D-band intensity.[37] The observed decrease in the D-band signal suggests that the interaction between CNH-N and MoS_2 is not limited to simple electrostatic attraction but may also involve stronger interfacial electronic coupling between the two components. Similar reductions in Raman defect-related intensity ratios have been reported in carbon-based hybrid materials, where charge transfer and interfacial chemical interactions modify the electronic structure and Raman scattering response of the carbon phase. Therefore, the observed decrease in I_D/I_G is consistent with the formation of a strongly electronically coupled CNH-N–MoS_2 heterostructure.

To further investigate the spatial distribution of these interactions, Raman mapping was performed over a 25 μm × 25 μm region of the CNH-N–MoS_2 hybrid (Fig. 3b,c). As shown in Fig. 3b, MoS_2-rich regions overlap preferentially with the edges of CNH-N aggregates. Correspondingly, the Raman map of the I_D/I_G ratio reveals values close to 1.15 in these overlapping regions, represented by the green areas. In contrast, isolated red domains within the CNH-N aggregates exhibit I_D/I_G values approaching 1.5, similar to those observed for the pristine CNH-N sample. These regions are attributed to CNH-N domains that are not in direct contact with MoS_2 nanosheets and therefore retain their original Raman characteristics. The spatial correlation between MoS_2 distribution and the decrease in the I_D/I_G ratio provides strong evidence for interfacial interactions between the two components. The Raman mapping results therefore support the successful assembly of the CNH-N–MoS_2 hybrid and suggest the presence of charge-transfer or chemical coupling effects at the CNH-N/MoS_2 interface.

The morphology, structure, and elemental composition of the synthesized nanostructures were investigated by a combination of TEM techniques, enabling analysis at the sub-nanometer scale (Fig. 4). Representative TEM images of CNH-N are shown in Fig. 4a and 4b, revealing spherical aggregates with diameters of approximately 50 nm. Notably, the outer edges of the CNHs are surrounded by a thin amorphous layer, which can be attributed to the presence of grafted TMA moieties on the CNH surface (Fig. 4b). Following hybridization, large exfoliated MoS_2 nanosheets with lateral dimensions of ~ 500 nm were observed to be decorated by and intimately associated with CNH-N aggregates (Fig. 4c). A higher-magnification image of the selected region (Fig. 4d) clearly demonstrates the close contact between CNH-N and MoS_2, indicating successful assembly of the heterostructure. Structural analysis of this region confirmed the presence of the metallic 1T phase of MoS_2, as evidenced by the high-resolution TEM image and corresponding fast Fourier transform (FFT) analysis shown in Fig. 4e and 4f.[35] Finally, the elemental distribution obtained by energy-dispersive X-ray spectroscopy (EDS) mapping (Fig. 4g) confirms the coexistence of carbon, molybdenum, and S within the same nanostructure, providing direct evidence for the successful integration of CNH-N and MoS_2 into the hybrid material.

Electrocatalytic ORR

Cyclic voltammetry (CV) measurements were first performed in O_2-saturated 0.1 M KOH solution to investigate the electrochemical behavior of the prepared materials (Fig. 5a). Pristine CNHs exhibited a

noticeably higher capacitive current than CNH-N, suggesting that functionalization with TMA groups occupies a significant fraction of the electrochemically active defect sites and surface functionalities present on the CNH surface. But considering the loading amount of the catalyst is the same, it is also possible that the actual weight of CNH in CNH-N is reduced, thus reducing the active sites. A similarly low capacitive current was observed for CNH-N–MoS_2, indicating that the surface properties of CNH-N are largely retained after hybrid formation. In contrast, the physical mixture of CNHs and MoS_2 displayed a capacitive response closer to that of pristine CNHs, consistent with the absence of covalent functionalization. All carbon-containing samples exhibited a redox feature centered at approximately 0.82 V vs. RHE. This signal has previously been associated with doping-induced charge delocalization and modifications of the spin density distribution within the sp^2 carbon network, which facilitate oxygen adsorption and O = O bond activation.[38] The persistence of this feature after functionalization and hybridization suggests that these active carbon sites remain electrochemically accessible. Pure MoS_2 displayed a redox process at approximately 0.80 V, which is attributed to the formation of adsorbed Mo–OH species.[39]

To evaluate the ORR activity, rotating disk electrode (RDE) measurements were performed (Fig. 5b). Pristine CNHs and CNH-N exhibited similar ORR onset potentials of approximately 0.72 V vs. RHE, indicating that surface functionalization alone does not significantly alter the ORR onset. In contrast, the CNH-N–MoS_2 heterostructure showed a substantially improved onset potential of 0.80 V. Furthermore, CNH-N–MoS_2 achieved a half-wave potential of 0.74 V, highlighting its superior electrocatalytic performance. To prove the synergistic effect between CNH-N and MoS_2 in the hybrid material thanks to the covalent functionalization and the electrostatic interactions, a physical mixture of CNHs and MoS_2 was prepared with the same MoS_2 content than in the hybrid material. As seen in Fig. 5b, the physical mixture exhibited an intermediate onset potential of 0.74 V, lying between those of pristine CNHs (0.72 V) and MoS_2 (0.77 V), which confirms the absence of any synergistic effect between the two in absence of any interaction.

Besides catalytic activity, the ORR pathway is another critical parameter for evaluating electrocatalyst performance. In alkaline media, ORR can proceed either through a two-electron pathway producing peroxide species or through the preferred four-electron pathway directly generating hydroxide ions:

$O_2 + H_2O + 2e^- \rightarrow HO_2^- + OH^-$ (U° = 0.76 V vs. RHE)

$O_2 + 2H_2O + 4e^- \rightarrow 4OH^-$ (U° = 1.23 V vs. RHE)

Because peroxide species can decrease energy efficiency and promote electrode degradation, minimizing their formation is highly desirable. Ring-disk measurements revealed that the ring current associated with peroxide generation was remarkably low for CNH-N–MoS_2, whereas substantially higher ring currents were observed for all other samples (Fig. 5c). This result indicates greatly suppressed peroxide formation on the heterostructure catalyst.

Quantitative analysis of the RRDE data further confirmed significant differences in the ORR mechanism (Fig. 5d and 5e). At 0.7 V vs. RHE, the number of electrons transferred (n) was approximately 3.8 for CNH-N–MoS_2, compared with 3.2 for CNH-N and 2.7–2.8 for pristine CNHs and MoS_2. These values correspond to peroxide yields of approximately 6%, 40%, 64%, and 61%, respectively. Therefore, ORR on CNH-N–MoS_2 proceeds predominantly through a quasi-four-electron pathway with minimal peroxide production, approaching the behavior of commercial Pt/C catalysts under similar conditions. In contrast, the individual components preferentially follow the less desirable two-electron pathway. The physical mixture of CNHs and MoS_2 exhibited an intermediate electron transfer number of approximately 3.3, demonstrating that simple mixing cannot reproduce the performance of the heterostructure. These results clearly indicate that the synergistic interaction established through covalent functionalization and electrostatic assembly is essential for promoting the selective four-electron ORR pathway.

Electrochemical impedance spectroscopy (EIS) was subsequently employed to investigate charge-transfer properties (Fig. 5f). All samples exhibited a similar high-frequency intercept of approximately 5 Ω, indicating comparable electrolyte resistance. The semicircular region of the Nyquist plots corresponds to the charge-transfer resistance (R_{ct}) and double-layer capacitance. Functionalization of CNHs resulted in a marked decrease in R_{ct} from 131.3 Ω for pristine CNHs to 73.5 Ω for CNH-N, demonstrating that the introduced functional groups facilitate interfacial charge transfer. An even lower R_{ct} of approximately 66 Ω was observed for CNH-N–MoS_2, comparable to that of pure MoS_2. Importantly, this value is substantially lower than that measured for the physical CNH + MoS_2 mixture (107 Ω), providing strong evidence that the intimate interfacial coupling between CNH-N and MoS_2 significantly enhances charge-transfer kinetics and accelerates ORR at the electrode–electrolyte interface.

Concisely, the CNH-N–MoS_2 outperforms the CNH-N, MoS_2 and mixed CNH+MoS_2 counterparts during the ORR tests, in terms of both catalytic activity and 4-electron pathway selectivity. The enhanced ORR performance of CNH-N–MoS_2 is attributed to the intimate coupling between the two components through covalent attachment and interfacial van der Waals interactions. These interactions facilitate charge transfer across the heterointerface, as evidenced by a much lower charge transfer resistance. In addition, they are also expected to optimize the adsorption energies of ORR intermediates and consequently affect the reaction pathways.

Computational modelling studies

To understand the influence of functionalization of CNHs in ORR pathways, we performed DFT based computations, on both electronic and catalytic properties of the heterojunctions with and without functionalized TMA (Fig. 6a). The electronic structure analysis points to a clear strengthening of interfacial charge redistribution after functionalization. The interface formation is responsible for a transfer of electron at the interface, from the CNH to the MoS_2 component. The TMA-modified CNH is more strongly adsorbed to the MoS_2 monolayer at a distance of 0.16 nm instead of 0.31 nm for pristine CNH (for more detail see Fig. S2 in SI). Bader charge analysis allows to quantify the electron transfer

upon the interface formation, confirming that the magnitude of this transfer is substantially larger for the modified system, going from a gain of 0.290 |e| in the CNH+MoS_2 model to up to 0.825 |e| for the CNH-N-MoS_2 interface, indicating a threefold increased propensity of electron transfer for the TMA modified heterojunction.[40] This trend is confirmed by the charge density difference shown in Fig. 6a, which provides a real-space visualization of electron depletion on the CNH side and electron accumulation on the MoS_2 side of the interface, which is strongly enhanced by the presence of the TMA.

These findings are also supported by the work function analysis. Although the total work function shift ($\Delta\phi$) remains nearly unchanged when comparing the two interfaces, varying from − 1.40 eV for CNH+MoS_2 to − 1.43 eV for CNH-N-MoS_2 its origin changes markedly. We consider the work function shift as the sum of two contributions:

$$\Delta\phi = CT + \Delta V_{SAM}$$

where CT represents the charge transfer upon the interface formation and ΔV_{SAM} the dipolar contribution of the CNH(-N) moiety. CNH+MoS_2 shows a negative ΔV_{SAM} contribution of − 0.87 eV, leading to a relatively small negative charge transfer term of value − 0.53 eV. The functionalization of CNH with the TMA leads to a reverse in direction of its dipole moment, which becomes positive and with a value of 2.12 eV, resulting in a CT term being much more significant and negative − 3.55 eV. Thus, the electronic properties analysis shows that the TMA modification of the interface favors the electron transfer process towards MoS_2. The negative shift in work function further confirms that the electrons injection barrier is decreased, and the large amount of CT on the TMA modified interface confirms its preference for the 4e- pathway for ORR over the $2e^-$ one.

To confirm this results, we performed further calculations on the catalytic activity of both interfaces and compare the propensity for both 2e- and 4e- pathways. The ORR intermediates — *OOH, *O, and *OH — were sequentially adsorbed on the selected S site of metallic 1T-MoS_2 at the interface. This approach is consistent with previous theoretical studies of MoS_2-based ORR systems, in which local electronic perturbations in sulfur-containing environments were shown to influence the oxygen reduction pathway.[41,42]

Figure 6b reports the Gibbs free energy diagram for the ORR on both heterojunctions, when an applied bias of 0.8 V is applied (results in absence of the bias are reported in Fig. S3). The 4e reaction path follow the classic intermediates formation, from O_2 adsorption to *OOH (where * indicate the catalytic substrate), *O, and *OH, while for the $2e^-$ reaction we consider the *OOH + H_2O -> *OH + H_2O_2 intermediate, from which the release of H_2O_2 will lead to the *OH intermediate which is the same as for the $4e^-$ pathway.

A first difference between the two models is their activity at zero bias, since CNH-N-MoS_2 follows almost perfectly the ideal catalyst (Fig. S4) for *OOH and *OH. However, both catalysts tend to strongly

bound the *O intermediate, and the difference in this adsorption energy is the potential determining step (PDS) of the reaction, and the key intermediate for the preference of the $4e^-$ over the $2e^-$ pathway for CNH-N-MoS_2. This strong absorption is reflected in the very short S-O bond, of 0.15 nm, compared to the longer *OOH and *OH bonds, with values in the 0.67–0.72 nm range (see Table S2-4 in SI). According to the Sabatier's principle, a too strong adsorption energy is detrimental for catalysis, since the adsorbate can poison the catalyst and the reaction become sluggish. For the interface between pure CNH and MoS_2, the overpotential of the $4e^-$ pathway arises to 1.43 eV, while for the concomitant $2e^-$ path only 1.00 eV is requested. Thus, the release of H_2O_2 towards the *OH intermediate is favored compared to the 4e- pathway through the *O intermediate, rationalizing the experimental finding of both H_2O_2 and water production on this catalyst.

The opposite scenario appears for the CNH-N-MoS_2 catalyst. Now, the formation of the 2e- key intermediate, *OH+ H_2O_2 requires an overpotential of 1.80 eV, while the classic $4e^-$ pathway through the formation of the *O intermediate requires a lower overpotential of 1.51 eV. Thus, the classic $4e^-$ pathway is the favored one for the TMA modified interface, rationalizing the selective water formation observed experimentally. This is further confirmed by the CT analysis on this PDS step, where a stronger electron depletion of -0.91 |e| is present on CNH-N-MoS_2 (compared to the − 0.43 |e| on CNH-MoS_2), leading to a larger electron accumulation on the *O intermediate of 1.18 |e| (compared to the 1.10 |e| on CNH-MoS_2), confirming the improved electron transfer kinetic on the functionalized interface.

Conclusions

In summary, this work demonstrates a successful strategy for constructing highly efficient CNH-N–MoS_2 heterostructures through a stepwise functionalization approach. By covalently introducing TMA groups onto CNHs and interfacing them with negatively charged 1T-MoS_2 nanosheets, robust electrostatic and chemical interactions are established. Comprehensive spectroscopic, thermal, and microscopic analyses confirm the effective bonding and structural integrity of the hybrid materials. The resulting CNH-N–MoS_2 heterostructure exhibits markedly enhanced electrocatalytic performance toward the oxygen reduction reaction, achieving a dominant four-electron pathway with ~ 94% selectivity to H_2O—comparable to commercial Pt/C catalysts. This superior activity is attributed to improved charge-transfer kinetics, stabilization of the metallic 1T phase of MoS_2, and the abundance of accessible catalytic sites facilitated by the functionalized CNH framework. Overall, these findings highlight the potential of covalently engineered carbon–TMDC heterostructures as promising, low-cost and critical raw materials-free alternatives for next-generation fuel cell cathode materials.

Experimental

Materials preparation CNHs were purchased from Carbonium S.r.l (batch number LA102048A-0). All the other reagents and solvents were purchased from Sigma Aldrich and used without further purification.

1T-MoS $_2$ Production 1T-MoS_2 was produced by a slightly modified lithiation procedure reported in the literature. A three-neck round bottom flask was connected to an Ar Schlenk line and cleaned following standard Schlenk line procedure (cycles of vacuum, heating, and Ar flux), after which 1 g of bulk MoS_2 and a magnetic stirrer were added under Ar flux in the round bottom flask and left drying under vacuum for 1 h at 40°C. After drying, the glassware was cooled down using an ice bath, and then 4 mL of dry hexane was added, using an Ar-purged syringe, to the glassware under moderate stirring. Subsequently, 6 mL of LinBut in hexane was added in a similar way to the round bottom flask. The ice bath then, was removed and the solution was left stirring for 3 days at room temperature. At the end of the reaction, the hexane solution was recuperated using hexane as a solvent and centrifuged at 6000 rpm for 20 min, removing the supernatant and adding fresh hexane each time. This procedure was performed three times, and the final tubes were left drying under vacuum at 40°C overnight. Subsequently, 800 mg of the as lithiated MoS_2 were added to 400 mL of deionized water and exfoliated using a tip-sonicator (TS, Bandelin Sonoplus), operating at 80% power output with 1 s on/1 s off cycles for 2 h while kept at 0°C with a nice bath. The suspension was then centrifuged at 6000 rpm for 20 min and the supernatant was kept for further work. Furthermore, a set amount was freeze-dried to obtain 1T-MoS_2 powder for further characterization and to calculate the concentration of the suspension, which was 1 mg/mL on average.

Synthesis of TMA functionalized CNHs (CNH-N) 30.0 mg (2.50 mmol) of CNH and 0.6947 g (2.50 mmol) of TMA iodide (synthetized according to a procedure reported in literature) were dispersed into 17 mL of milli-Q water.[31] The mixture was heated to 80°C under N2 flow and magnetic stirring. Then 353 µL of isopentyl nitrite (2.50 mmol) were added. After 4 hours the reaction mixture was cooled to room temperature. The dispersion was filtered on a polycarbonate Isopore filter with 0.1 µm porosity. The product was washed with five 25 mL aliquots of a mixture of methanol and MilliQ water (2:3) and five 25 mL aliquots of methanol. The functionalized product was removed from the filter by sonication in methanol and was dried under nitrogen flow.

Synthesis of the hybrid materials For CNH-N-MoS_2, 10 mg of CNH-N were dispersed in 10 mL of milli-Q water through bath sonication for 1 minute. The CNH-N dispersion was mixed with 1 mL of 1T MoS_2 dispersion in water with a concentration of 1 mg/mL. The mixture was decanted for 20 h and subsequently centrifugated at 5000 rpm for 5 minutes. The supernatant was removed, and the solid product was dried under a nitrogen flow. For CNH+MoS_2, 10 mg of CNHs and 1 mL of MoS_2 are mixed by both sonication, then centrifuge at 5000 rpm for 5 minutes. The weight ratio of MoS_2 in both hybrid materials is 10%.

Structural, Chemical, and Morphological Characterization DLS measurements were carried out on a Zetasizer Nano S analyzer (Malvern Instruments, Malvern, UK). The measurement angle was set at 173°, backscatter (NIBS default). The analyses were carried out in a low volume disposable plastic cuvette with a 1 cm optical path, in water at 25°C, waiting an equilibration time of 120 seconds. The resulting value is an average of 3 measurements of 11 runs each, with a run duration of 10 seconds. Zeta Potential measurements were carried out in a clear disposable zeta cell, in NaCl 30 mM at 25°C, waiting

an equilibration time of 120 seconds. The theoretical model set for the measurement was the Smoluchowski equation. The resulting value is an average of 3 measurements of 10–100 runs each. To prepare the sample for DLS and Z potential, 5 mg of CNH-N were dispersed in 2.5 mL of Milli-Q water by pulsed microtip sonication for 1 minute and subsequent centrifugation at 10000 rpm for 10 min. The supernatant was recovered and filtered over cotton wool. The obtained dispersion, which concentration was defined as the water dispersibility of CNH-N, was used to perform DLS and Z potential measurement. TGA measurements were carried out on a TGA Q5000IR of TA instruments (TA instruments, New Castle, DE, USA). The analyses were performed on a 100 µL Platinum-HT TGA pan in N_2 atmosphere. The measurement method consists of an isotherm at 100°C for 10 minutes followed by a 10°C/min ramp to 1000°C. TRIOS software has been used to process the thermograms. The concentration of CNH-N in water was evaluated by drop casting 1 mL of the CNH-N dispersion on a calibrated TGA pan and then running an isotherm in air at 100°C until constant weight. Raman spectra have been acquired with an Invia Renishaw Raman microspectrometer (20x objective). The solid samples were deposited on glass micro slides. The measurements were performed by irradiating the sample with a 633 nm He-Ne laser at room temperature for a time of 10s. We characterized samples using a WITec confocal Raman system (α300-Raman WITec GmbH, Ulm, Germany), equipped with a 100X Zeiss objective, NA = 0.9 and a dispersive grating of 600 gr/mm that images a 100 µm core fiber, used to couple microscope to the f = 320 mm spectrometer, as the input slit aperture on a 1 × 2048 pixels CCD (Newtown CCD, Andor, -80°C thermoelectric cooled). A solid-state laser, 532 nm, power of 14 mW, was used as the excitation line. The samples were dropped on n-type Si wafer. For the Raman spectra, each measure was obtained accumulating 80 spectra, each with an integration time of 25 s. Raman spectroscopy maps of 4 × 4 µm and 48 × 48 points were acquired at 2 seconds integration time per point. XPS spectra were acquired using a spectrometer manufactured by Physical Electronics GmbH (PHI 5000 VersaProbe II). TEM and HRTEM imaging was performed on a TALOS F200X (Thermo Fisher Scientific, Eindhoven, Netherlands) instrument without aberration correction, operating at an acceleration voltage of 200 kV. Images were captured using a 16-megapixel CMOS cam- era, and the FFT pattern was processed with Velox software (Thermo Scientific Velox Software, Thermo Fisher Scientific Inc., Waltham, MA, USA). Samples were prepared by dropping dilute suspensions ofnanoma- terials in ethanol onto carbon film-coated 200 mesh copper grids.

Electrochemical characterization Electrochemical measurements were conducted in a three-electrode cell using a mercury-mercury oxide as reference electrode and a graphite rod as counter electrode. A RRDE tip with a glassy carbon (GC) disk (5 mm diameter) and a platinum ring was used as working electrode. A thin-film catalyst layer was deposited by drop-casting on the GC electrode. The catalyst ink was prepared by mixing 2 mg of catalyst, 20 µL Nafion® (5 wt.%, Sigma-Aldrich), 50 µL ethanol and 450 µL Milli-Q water. The ink was sonicated for 20 min to facilitate the dispersion of the catalyst and then, an aliquot of 10 µL was deposited on the GC. Linear sweep voltammetry (LSV) measurements in Ar- and O_2-saturated 0.1 M KOH (Sigma-Aldrich) were carried out to determine the activity towards the ORR. Then, LSVs were recorded at different rotation rates at 10 mV s^{-1} in O_2-saturated 0.1 M KOH, while holding the Pt ring at + 0.4 V, to determine the number of electrons transferred (n) and the percentage of hydrogen

peroxide anion (HO_2^-) formed. The fraction of current due to HO_2^- that is recorded by the ring electrode ($\%HO_2^-$) and the corresponding electron transfer number during ORR (ne^-) were calculated by using the following equations:

$$\%HO_2^- = 100 \frac{2\varvec{I}\varvec{r}}{\varvec{I}\varvec{d}\varvec{N} + \varvec{I}\varvec{r}} \quad \text{[Eq. 1]}$$

$$n = \frac{4\varvec{I}\varvec{d}\varvec{N}}{\varvec{I}\varvec{d}\varvec{N} + \varvec{I}\varvec{r}} \quad \text{[Eq. 2]}$$

where Ir is the ring current, Id is the disk current, and N is the collection efficiency (0.249). Currents reported are normalized by the electrode geometrical area (0.196 cm^2)

Computational studies To gain insight into the origin of the improved ORR selectivity of CNH-N–MoS_2, periodic density functional theory calculations (DFT) were performed with VASP within the plane-wave PAW formalism.[43] The CNH was described as a curved cone-like fragment which is appropriate for carbon nanohorns and better reflects their local topology and as a result electronic structure.[44] The modified system contained one phenyltrimethylammonium (TMA) group covalently attached to the tip of the CNH.

All calculations were performed in vacuum using a hexagonal supercell with in-plane lattice parameters of 19.14 Å and a cell height of 36 Å. To eliminate polarization effects between the MoS2 monolayer and the CNH, vacuum layers with thicknesses of 21 Å and 15 Å were introduced above the systems. The initial interface structure was relaxed using a cutoff of 10 − 5 eV for the total energy and 0.01 eV/Å for the maximum force. Dispersion corrections implemented in VASP were included to account for van der Waals interactions.[45] For the Bader charge analysis, the core electron densities were additionally reconstructed and included in the calculations. To visualize the Bader charge distribution, the charge density difference was calculated according to the equation:

$$\Delta\rho(r) = \rho(r)_{CNH/1T\text{-}MoS2} - \rho(r)_{CNH} - \rho(r)_{MoS2}$$

To obtain the Gibbs free energies of the ORR elementary reaction steps at 298 K, the Computational Hydrogen Electrode (CHE) framework was employed. The CHE model is one of the most widely used theoretical frameworks in electrocatalysis modeling. The CHE approach enables the calculation of electrochemical reaction free energies using DFT without explicitly modeling solvated protons and electrons. In this method, the chemical potential of a proton–electron pair is referenced to one-half of the chemical potential of gaseous hydrogen under standard conditions, according to the equilibrium:

$$H^+ + e^- = 1/2\ H_2$$

This simplification enables the evaluation of reaction energetics as a function of electrode potential and pH according to the following equation:

$G(T) = E_0 + E_{ZPE} - TS + eU - 2.3\ RT/F\ pH$

where E0 is the electronic energy obtained from DFT calculations, EZPE is the zero-point energy correction, TS is the entropy contribution, U is the applied electrode potential.[46–48] During the structural optimization of the reaction intermediates, only the adsorbate and atoms up to the second nearest neighbor of the sulphur active-site S atom were allowed to relax, while all remaining atoms were constrained to their equilibrium positions. Geometry optimizations in gas phase were followed by a single point calculation in which water solvent was considered with the PCM model. To obtain the vibrational contributions required for the calculation of ΔG of the reaction steps, a series of phonon calculations was performed using the frozen phonon approach. Atomic displacements of 0.015 Å were applied to construct the force constant matrix and evaluate the vibrational properties of the systems. During the phonon calculations, only the adsorbate and active site region were allowed to vibrate, whereas all other atoms were kept fixed. This approximation reduced the computational cost while preserving the local structural and electronic environment relevant to the adsorption process and catalytic activity.

Declarations

Conflicts of interest

There are no conflicts to declare.

Author Contribution

M.W. performed conceptualization, data curation, Raman mapping measurement and analysis, investigation, wrote the original draft, reviewed, and edited the final manuscript. S.B. performed the Raman spectra and analysis. L. Cieszyński and S.O. performed DFT calculations, reviewed and edited the manuscript. M.C. synthesized 1T MoS2 and performed XPS measurement. M.P., Y.W. and Y.Z. reviewed and edited the manuscript. L. Calvillo performed ORR measurements, the XPS analysis, reviewed and edited the manuscript. E.M., J.Z. and T.G. provided resources, reviewed, and edited the final manuscript.

Acknowledgements

This work was supported by the European Research Council through project JANUS BI (ID: 101041229). S.O. thanks the Polish National Science Centre for funding (grant number UMO-2023/50/E/ST4/00197). We gratefully acknowledge the Polish high-performance computing infrastructure PLGrid (HPC Center: ACK Cyfronet AGH) for providing computer facilities and support within the computational grant number PLG/2026/019113. E.M. thanks the University of Padova (P-DiSC#07BIRD2026-UNIPD) for funding.

Data availability

All data supporting the conclusions of this work are presented in the main article. Raw data are available from the corresponding author upon reasonable request.

References

1. León, M. I., Romero-Castañón, T., Flores-Hernández, J. R. & Nava, J. L. Experimental determination of HOR and ORR kinetic parameters in an AEMFC by the distribution of relaxation times method. *Journal of Power Sources* 629, 236000 (2025).
2. Baglio, V., Martínez-Arias, A., Helsel, N. & Choudhury, P. Non-Platinum Group Metal Oxygen Reduction Catalysts for a Hydrogen Fuel Cell Cathode: A Mini-Review. *Catalysts 2025, Vol. 15, Page 588* 15, 588 (2025).
3. Lee, J.-W. *et al.* Atomic-scale vacancy engineering unlocks basal-plane catalytic activity in metallic WSe2 for reversible oxygen electrocatalysis. *Materials Science and Engineering: R: Reports* 169, 101190 (2026).
4. Meng, F. *et al.* Rapid synthesis of single-layer iron-doped 2H tungsten sulfide via magnetic induction heating for piezocatalytic reduction of oxygen to hydrogen peroxide. *Applied Catalysis B: Environment and Energy* 371, 125224 (2025).
5. Pozzati, M. *et al.* Systematic Investigation on the Surfactant-Assisted Liquid-Phase Exfoliation of MoS2 and WS2 in Water for Sustainable 2D Material Inks. *physica status solidi (RRL) – Rapid Research Letters* 2400039 (2024) doi:10.1002/PSSR.202400039.
6. Rowley-Neale, S. J., Smith, G. C. & Banks, C. E. Mass-Producible 2D-MoS2-Impregnated Screen-Printed Electrodes That Demonstrate Efficient Electrocatalysis toward the Oxygen Reduction Reaction. *ACS Applied Materials and Interfaces* 9, 22539–22548 (2017).
7. Xu, H. *et al.* Two-Dimensional MoS2: Structural Properties, Synthesis Methods, and Regulation Strategies toward Oxygen Reduction. *Micromachines 2021, Vol. 12, Page 240* 12, 240 (2021).
8. Ma, Y. *et al.* Enhanced Activities in Alkaline Hydrogen and Oxygen Evolution Reactions on MoS2 Electrocatalysts by In-Plane Sulfur Defects Coupled with Transition Metal Doping. *Small* 18, 2203173 (2022).
9. Upadhyay, S. N., Kumar, V., Sharma, N. & Pakhira, S. Enhanced Catalytic Performance of Vanadium-Doped MoS2 as a Multifunctional Electrocatalyst toward ORR, OER, and HER Applications. *ACS Applied Energy Materials* 8, 8937–8949 (2025).
10. Boll, F. *et al.* In situ growth of layered 1T-MoS 2 onto carbon nanofibers as a strategy towards advanced hybrid materials for electrochemical energy storage and catalysis. *Nanoscale* 17, 10706–10717 (2025).
11. Upadhyay, S. N., Joshi, H., Sharma, N. & Pakhira, S. Two-dimensional materials as emerging electrocatalysts for the HER, ORR, and OER: design strategies, challenges, and prospects in

sustainable energy conversion. *Physical Chemistry Chemical Physics* https://doi.org/10.1039/D6CP00222F (2026) doi:10.1039/D6CP00222F.

12. Amiinu, I. S. *et al.* Multifunctional Mo–N/C@MoS2 Electrocatalysts for HER, OER, ORR, and Zn–Air Batteries. *Advanced Functional Materials* 27, 1702300 (2017).
13. Chua, X. J. *et al.* Negative Electrocatalytic Effects of p-Doping Niobium and Tantalum on MoS2 and WS2 for the Hydrogen Evolution Reaction and Oxygen Reduction Reaction. *ACS Catalysis* 6, 5724–5734 (2016).
14. Shrivastav, M., Kumar, V., Rana, K. & Dhiman, R. Oxygen reduction reaction kinetics of 2H-MoS2 and mixed-phase 1T/2H-MoS2 as a metal-free cathodic catalyst for PEM fuel cells. *Journal of Applied Electrochemistry 2024 54:7* 54, 1517–1529 (2024).
15. Sebastian, M. M., Velayudham, P., Schechter, A. & Kalarikkal, N. Spinel Nickel Ferrite Nanoparticles Supported on a 1T/2H Mixed-Phase MoS2 Heterostructured Composite as a Bifunctional Electrocatalyst for Oxygen Evolution and Oxygen Reduction Reactions. *Energy & Fuels* 36, 7782–7794 (2022).
16. Meng, H. *et al.* Hybridization of iron phthalocyanine and MoS2 for high-efficiency and durable oxygen reduction reaction. *Journal of Energy Chemistry* 71, 528–538 (2022).
17. Wang, T. *et al.* Synergistic catalytic effect of MoS2 nanoparticles supported on gold nanoparticle films for a highly efficient oxygen reduction reaction. *ChemCatChem* 6, 1877–1881 (2014).
18. Jayabal, S. *et al.* Understanding the high-electrocatalytic performance of two-dimensional MoS 2 nanosheets and their composite materials. *Journal of Materials Chemistry A* 5, 24540–24563 (2017).
19. Saini, R., Naaz, F., Bashal, A. H., Pandit, A. H. & Farooq, U. Recent advances in nitrogen-doped graphene-based heterostructures and composites: mechanism and active sites for electrochemical ORR and HER. *Green Chemistry* 26, 57–102 (2024).
20. Hao, L. *et al.* Nitrogen-doped MoS2/carbon as highly oxygen-permeable and stable catalysts for oxygen reduction reaction in microbial fuel cells. *Journal of Power Sources* 339, 68–79 (2017).
21. Moghaddam, M. S., Bahari, A. & Litkohi, H. R. Using the synergistic effects of MoS2/rGO and bimetallic hybrids as a high-performance nanoelectrocatalyst for oxygen reduction reaction. *International Journal of Hydrogen Energy* 48, 33139–33154 (2023).
22. Zhang, S. *et al.* A defect-rich ultrathin MoS 2 /rGO nanosheet electrocatalyst for the oxygen reduction reaction. *RSC Advances* 11, 24508–24514 (2021).
23. Vinoth, R. *et al.* Synergistically Enhanced Electrocatalytic Performance of an N-Doped Graphene Quantum Dot-Decorated 3D MoS2–Graphene Nanohybrid for Oxygen Reduction Reaction. *ACS Omega* 1, 971–980 (2016).
24. He, C. *et al.* Oxygen Reduction Reaction Promoted by the Strong Coupling of MoS2 and SnS. *ACS Applied Energy Materials* 4, 9498–9506 (2021).
25. Liu, X., Ying, Y. & Ping, J. Structure, synthesis, and sensing applications of single-walled carbon nanohorns. *Biosensors and Bioelectronics* 167, 112495 (2020).

26. Swain, M. *et al.* Synergistic enhancement in energy storage in lithium/sodium ion batteries using engineered composites of MXenes and carbon nanohorns. *Nanoscale* 17, 26077–26094 (2025).
27. Zafar, A., Ji, Z., Marco-Guimbao, J. & Delgado, J. L. Functional Carbon Nanomaterials in Perovskite-Based Solar Cells: From Fullerenes to Carbon Nanohorns. *ACS Applied Electronic Materials* 7, 6721–6732 (2025).
28. Feng, T. *et al.* Functionalized Multi-Walled Carbon Nanotube Enhanced Myogenic Differentiation for Aligned Topography-Induced Skeletal Muscle Engineering. *Small* 21, 2504992 (2025).
29. Quaternary ammonium-functionalized carbon nanotubes/alginate nanocomposite hydrogels support myoblast growth and differentiation - Journal of Materials Chemistry B (RSC Publishing) DOI:10.1039/D5TB00601E. https://pubs.rsc.org/en/content/articlehtml/2025/tb/d5tb00601e.
30. Suarato, G. *et al.* Modified Carbon Nanotubes Favor Fibroblast Growth by Tuning the Cell Membrane Potential. *ACS Applied Materials & Interfaces* 16, 3093–3105 (2024).
31. Hadad, C. *et al.* Positive graphene by chemical design: tuning supramolecular strategies for functional surfaces. *Chemical Communications* 50, 885–887 (2013).
32. Tosin, E., Gatti, T., Agnoli, S., Calvillo, L. & Menna, E. Nitrogen- and Fluorine-Doped Carbon Nanohorns as Efficient Metal-Free Oxygen Reduction Catalyst: Role of the Nitrogen Groups. *Surfaces 2023, Vol. 6, Pages 227–238* 6, 227–238 (2023).
33. Pagona, G., Katerinopoulos, H. E. & Tagmatarchis, N. Synthesis, characterization, and photophysical properties of a carbon nanohorn–coumarin hybrid material. *Chemical Physics Letters* 516, 76–81 (2011).
34. Pagona, G., Karousis, N. & Tagmatarchis, N. Aryl diazonium functionalization of carbon nanohorns. *Carbon* 46, 604–610 (2008).
35. Crisci, M. *et al.* Easy Direct Functionalization of 2D MoS2 Applied in Covalent Hybrids with PANI as Dual Blend Supercapacitive Materials. *Advanced Materials Interfaces* 2400621 (2024) doi:10.1002/ADMI.202400621.
36. Domenici, S. *et al.* Hybrid Piezoresistive 2D MoS2/PEGDA/PANI Covalent Hydrogels for the Sensing of Low-to-Medium Pressure. *Small Structures* 2400131, (2024).
37. Gatti, T. *et al.* A D-π-A organic dye – Reduced graphene oxide covalent dyad as a new concept photosensitizer for light harvesting applications. *Carbon* 115, 746–753 (2017).
38. Lu, S., Shi, Y. & Zhang, B. Active Sites of Metal-Free Carbon Materials in Energy Electrocatalysis. *Advanced Materials* e73313 (2026) doi: 10.1002 /ADMA.73313;PAGE:STRING:ARTICLE/CHAPTER.
39. Karmodak, N. & Andreussi, O. Oxygen Evolution on MoS2 Edges: Activation through Surface Oxidation. *The Journal of Physical Chemistry C* 125, 10397–10405 (2021).
40. Henkelman, G., Arnaldsson, A. & Jónsson, H. A fast and robust algorithm for Bader decomposition of charge density. *Computational Materials Science* 36, 354–360 (2006).

41. Revolutionizing ORR catalyst design through computational methodologies and materials informatics - EES Catalysis (RSC Publishing) DOI:10.1039/D4EY00104D. https://pubs.rsc.org/en/content/articlehtml/2024/ey/d4ey00104d.
42. Liu, C., Dong, H., Ji, Y., Hou, T. & Li, Y. Origin of the catalytic activity of phosphorus doped MoS2 for oxygen reduction reaction (ORR) in alkaline solution: a theoretical study. *Scientific Reports 2018 8:1* 8, 13292- (2018).
43. Kresse, G. & Joubert, D. From ultrasoft pseudopotentials to the projector augmented-wave method. *Physical Review B* 59, 1758 (1999).
44. Karousis, N., Suarez-Martinez, I., Ewels, C. P. & Tagmatarchis, N. Structure, Properties, Functionalization, and Applications of Carbon Nanohorns. *Chemical Reviews* 116, 4850–4883 (2016).
45. Grimme, S., Antony, J., Ehrlich, S. & Krieg, H. A consistent and accurate ab initio parametrization of density functional dispersion correction (DFT-D) for the 94 elements H-Pu. *Journal of Chemical Physics* 132, 154104 (2010).
46. Alfonso, D. R., Tafen, D. N. & Kauffmann, D. R. First-Principles Modeling in Heterogeneous Electrocatalysis. *Catalysts 2018, Vol. 8, Page 424* 8, 424 (2018).
47. Rossmeisl, J., Nørskov, J. K., Taylor, C. D., Janik, M. J. & Neurock, M. Calculated Phase Diagrams for the Electrochemical Oxidation and Reduction of Water over Pt(111). *Journal of Physical Chemistry B* 110, 21833–21839 (2006).
48. Nørskov, J. K. *et al.* Origin of the Overpotential for Oxygen Reduction at a Fuel-Cell Cathode. *The Journal of Physical Chemistry B* 108, 17886–17892 (2004).

Figures

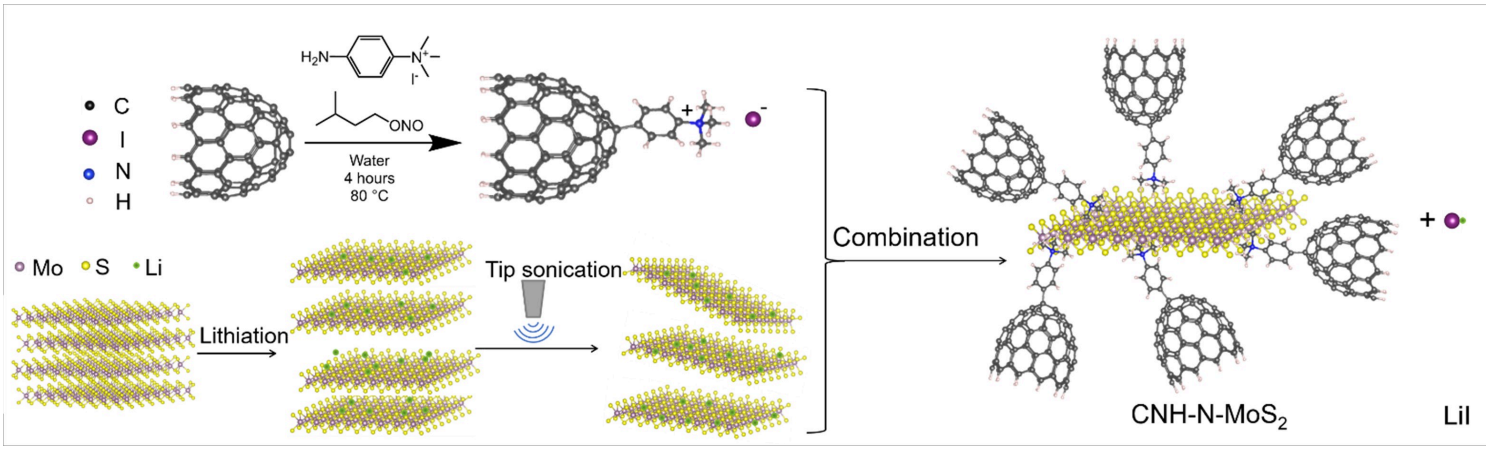


Figure 1

Synthetic illustration of the preparation of CNH-N-MoS_2 heterostructure.

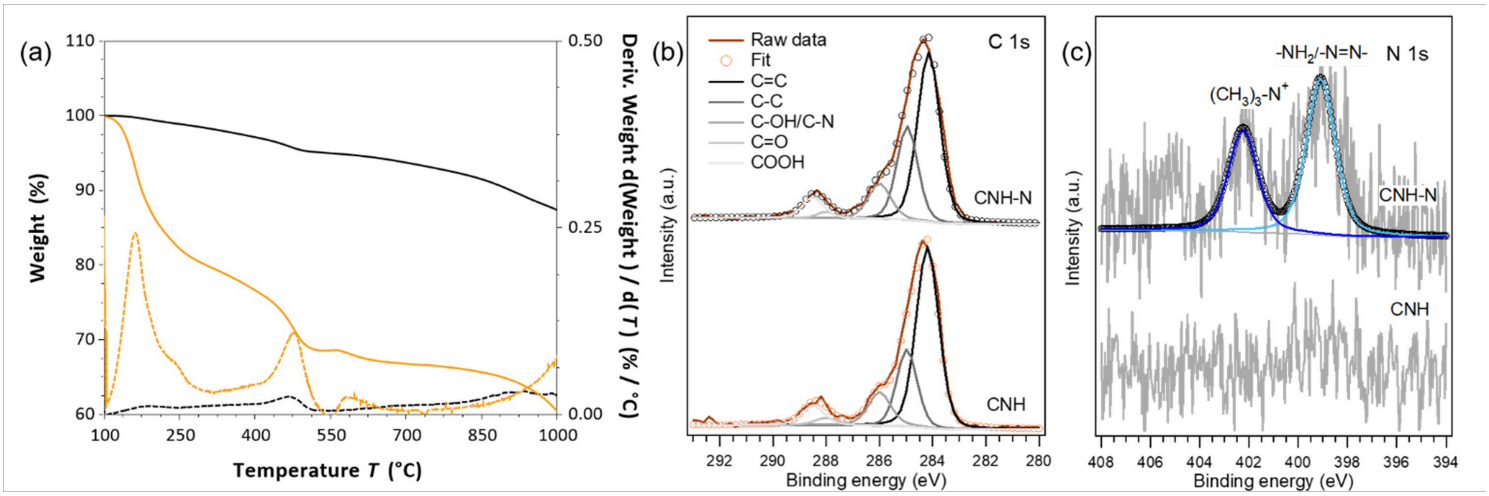


Figure 2

(a) Thermograms of CNH (black line) and CNH-N (red line). (b) C 1s and (c) N 1s XPS spectra of CNH and CNH-N.

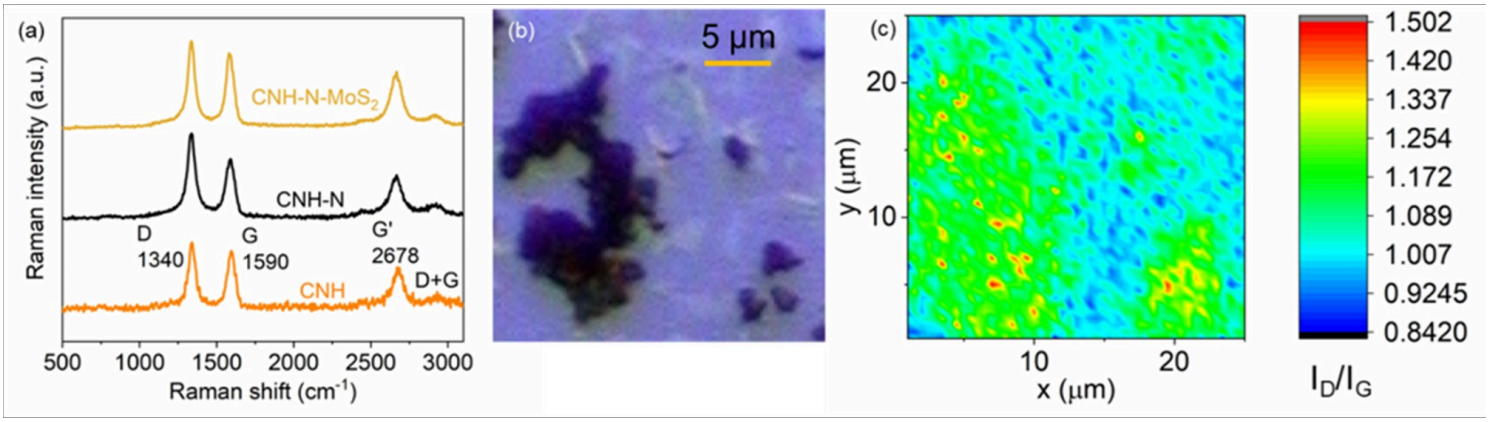


Figure 3

(a) Raman spectra of CNH-N-MoS_2, CNH-N and CNH. At the selected area (b), (c) Raman mapping of the peak ratio of I_D/I_G.

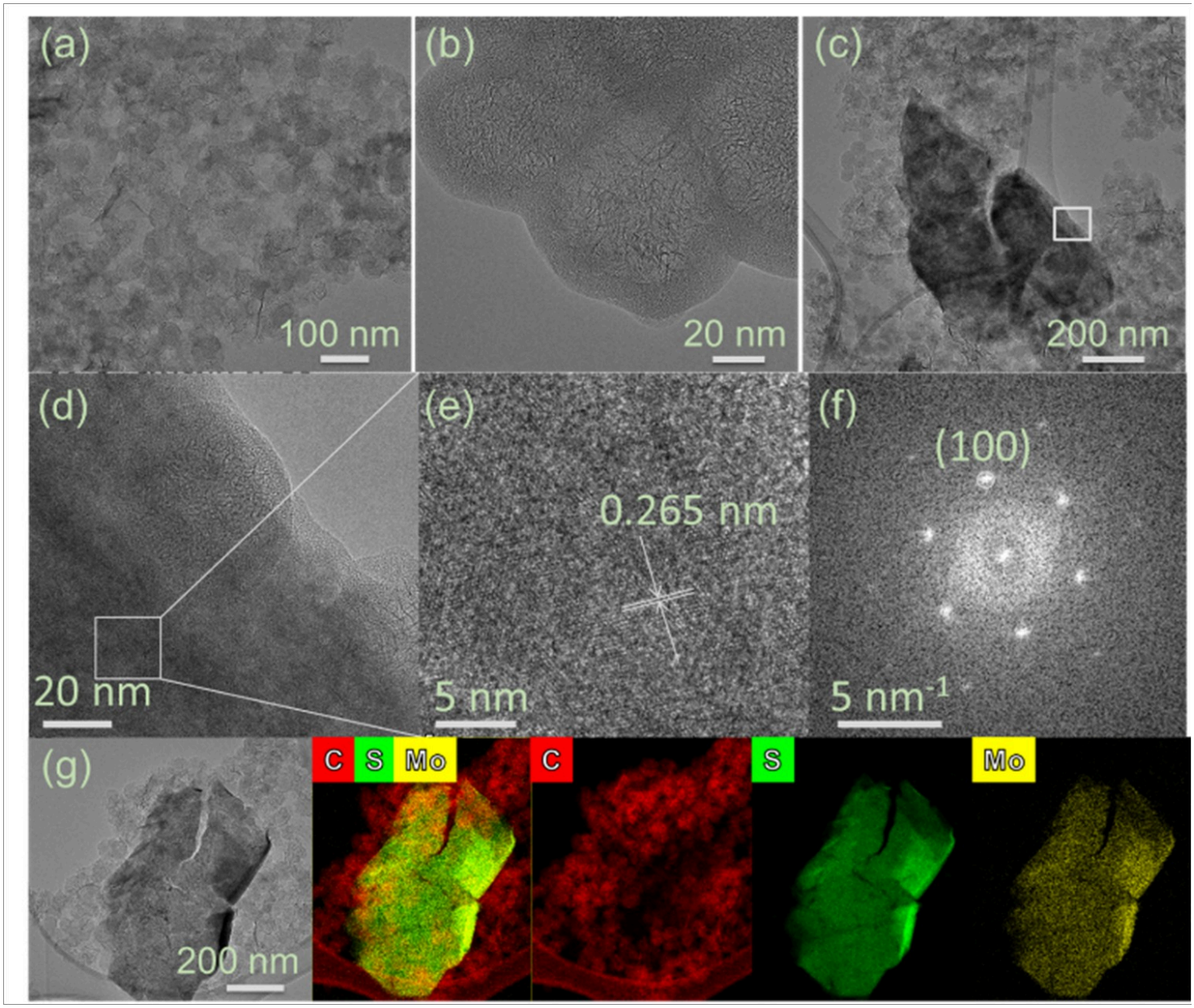


Figure 4

(a) low-magnification and (b) high-magnification TEM micrographs of CNH-N. (c) TEM image of the CNH-N-MoS_2 heterostructure. (d) HRTEM image taken from the white square in figure (c). (e) Lattice fringe from image (d) and the corresponding Fourier Transform from image (e) is shown in figure (f). (g) STEM image showing one of these CNH-N-MoS_2 heterostructures.

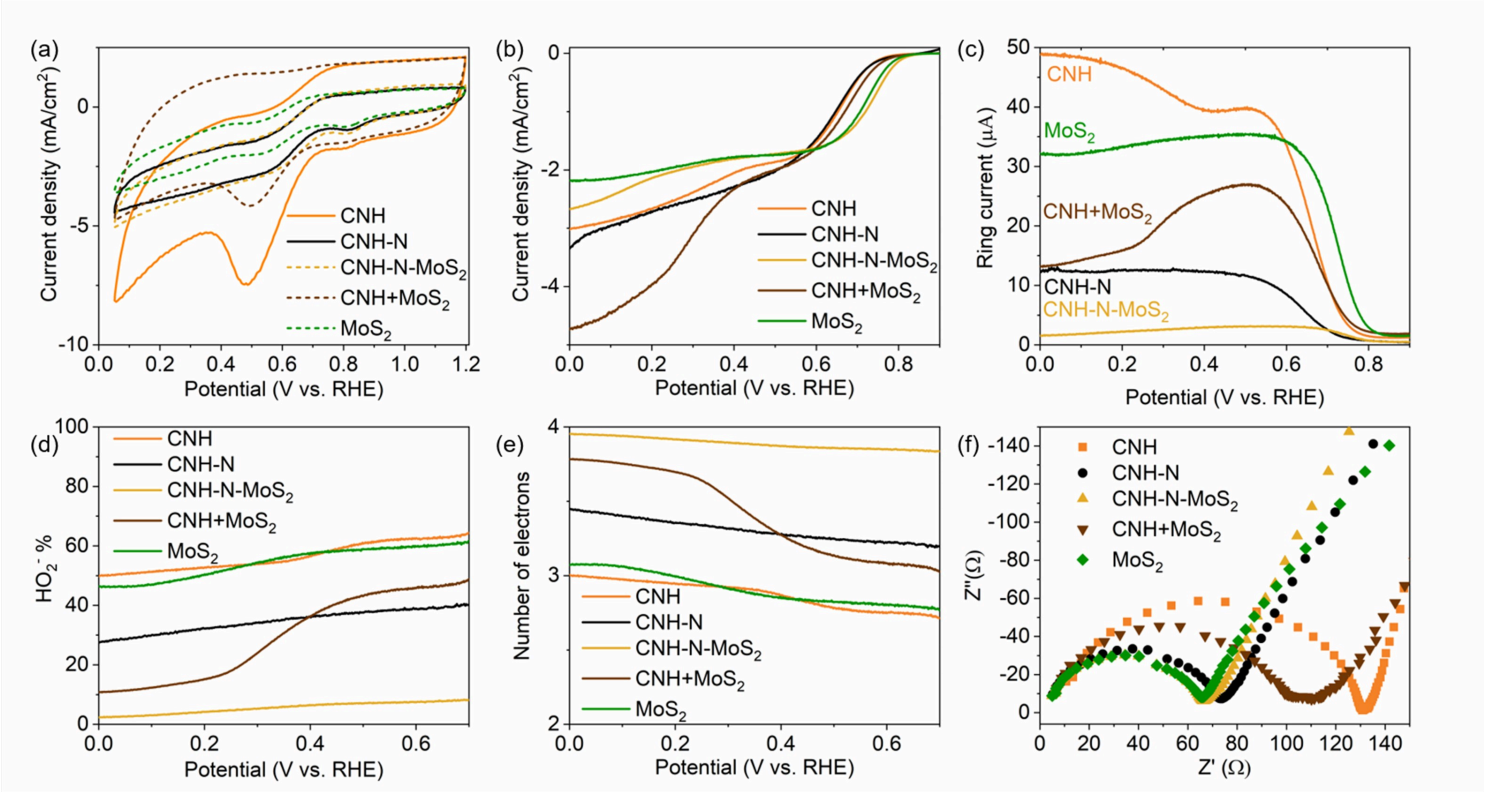


Figure 5

(a) CV in O_2-saturated KOH (0.1 M), (b) RRDE measurements in O_2-saturated 0.1M KOH at 1600 rpm, (c) corresponding ring current, (d) the corresponding selectivity to HO_2^-, (e) number of exchanged electrons as a function of the applied potential, and (f) EIS spectra of all the samples.

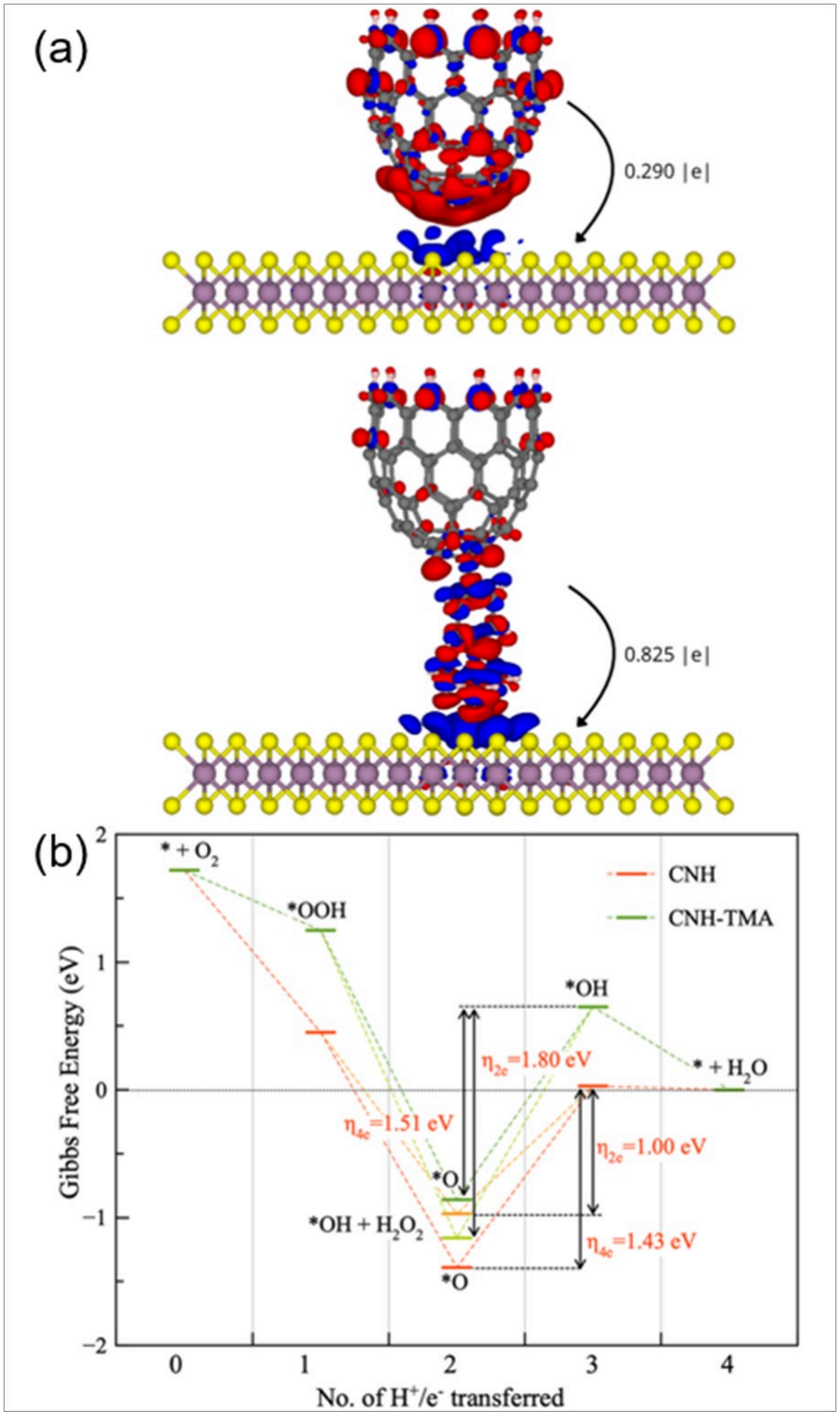


Figure 6

(a) Charge density difference for CNH-MoS_2 (top) and CNH-N-MoS_2 (bottom). Blue – electron density accumulation, red – hole density accumulation. (b) Gibbs free diagram for the ORR on both CNH-MoS_2 (red) and CNH-N-MoS_2 (green) catalysts, at an applied bias of 0.8 V and pH=13. Light green and orange symbols refer to the $2e^-$ pathway, red and green to the 4e pathway. The overpotential is reported in red.

Supplementary Files

This is a list of supplementary files associated with this preprint. Click to download.

- SupplementaryInformation2.docx